Mechano-chemical polarization of contiguous cell walls shapes plant pavement cells

Majda M.[1], Grones P.[1], Sintorn I.M.[2], Vain T.[1], Milani P.[3], Krupinski P.[4], Zagórska-Marek B.[5], Viotti C.[6,7], Jönsson H.[4,8,9], Mellerowicz E.J.[1], Hamant O.[3] and Robert S.[1*].

[1]Umeå Plant Science Centre (UPSC), Department of Forest Genetics and Plant Physiology, Swedish University of Agricultural Sciences, 901 83 Umeå, Sweden.

[2]Centre for Image Analysis, Uppsala University, Box 337, SE-751 05 Uppsala, Sweden.

[3] Laboratoire Reproduction et Développement des Plantes, Université de Lyon, ENS de Lyon, UCB Lyon 1, CNRS, INRA, F-69342, Lyon, France.

[4]Computational Biology and Biological Physics, Department of Astronomy and Theoretical Physics, Lund University, Sölvegatan 14A, SE-223 62 Lund, Sweden.

[5]Department of Plant Developmental Biology, Institute of Experimental Biology, University of Wrocław, Kanonia 6/8, 50-328 Wrocław, Poland.

[6]Umeå Plant Science Centre (UPSC), Department of Plant Physiology, Umeå University, 90187 Umeå, Sweden.

[7]Institute of Biochemistry and Biology, Plant Physiology, University of Potsdam, 14476 Potsdam, Germany.

[8]Sainsbury Laboratory, University of Cambridge, Bateman Street Cambridge CB2 1LR, United Kingdom.

[9]Department of Mathematics and Theoretical Physics, University of Cambridge, Wilberforce Rd, Cambridge CB3 0WA, United Kingdom.

*Correspondence should be addressed to: Stephanie.Robert@slu.se; Phone: +46 (0)90-786 8609; Fax: +46 90 786 8165.

*The lead contact: Stephanie.Robert@slu.se

Summary

The epidermis of aerial plant organs is thought to be limiting for growth, as it acts as a continuous load-bearing layer, resisting tension. Leaf epidermis contains jigsaw puzzle piece-shaped pavement cells whose shape has been proposed to be a result of subcellular variations in expansion rate that induce local buckling events. Paradoxically, such local compressive buckling should not occur given the tensile stresses across the epidermis. Using computational modeling, we show that the simplest scenario to explain pavement cell shapes within an epidermis under tension must involve mechanical wall heterogeneities across and along the anticlinal pavement cell walls between adjacent cells. Combining genetics, atomic force microscopy, and immunolabeling, we demonstrate that contiguous cell walls indeed exhibit hybrid mechano-chemical properties. Such biochemical wall heterogeneities precede wall bending. Altogether, this provides a possible mechanism for the generation of complex plant cell shapes.

Introduction

Because epidermis and epithelia are usually mechanically limiting for growth, they are essential for shaping organisms (Bai et al., 2010; Dyson et al., 2014; Kutschera and Niklas, 2007; Marcotrigiano, 2010; Savaldi-Goldstein and Chory, 2008; Savaldi-Goldstein et al., 2007; Swarup et al., 2005). Epidermal layers also display the intrinsic heterogeneity of the composing cells. In plants, adjacent cells within the epidermis can grow with various rates and directions (Elsner et al., 2012; Uyttewaal et al., 2012). Growth heterogeneity has also been proposed to occur at a subcellular scale. In particular, the presence of jigsaw puzzle shaped cells in certain types of plant epidermis has been proposed to rely on subcellular variations in expansion rate, inducing local buckling events (Fu et al., 2002, 2005). More specifically, the growth in these cells is associated with a stereotypical cytoskeleton pattern: cortical microtubules converge in the neck regions (indentations) and further mechanically reinforce the cell wall *via* the guided deposition of stiff cellulose microfibrils, thus locally restricting growth, while actin filaments accumulate on the opposite side, where a lobe is forming (Armour et al., 2015; Fu et al., 2002; Sampathkumar et al., 2014). This multipolar pattern is governed by small Rho GTPases (ROP for Rho of Plants), which also display a polar distribution: ROP6, *via* ROP-INTERACTIVE CRIB MOTIF-CONTAINING PROTEIN 1 (RIC1) and katanin activity, promotes the formation of the dense

network of microtubules in the necks, while ROP2, *via* RIC4, organizes the network of actin filaments in the lobes (Fu et al., 2005; Lin et al., 2013). While our understanding of the molecular players involved in the formation of these multipolar cells is quite advanced, one is left with a mechanical paradox. To some extent, the actin-enriched lobes have been compared to the tips of root hairs or pollen tubes, suggesting that cells would push each other. The presence of strong tensile stresses in the entire epidermis (Kutschera and Niklas, 2007; Sampathkumar et al., 2014) should however hinder such buckling events (Sampathkumar et al., 2014).

Here we revisit this question, taking the viewpoint of the cell wall, and we explore the possibility that such a cell shape emerges from locally established cell wall properties, while being constantly under tension. Pavement cells are surrounded by periclinal (parallel to the leaf surface) and anticlinal (perpendicular to the leaf surface) walls. The role of periclinal cell walls in maintaining cell shape is already well documented and involves a response of cortical microtubules to tension in the outer wall (Sampathkumar et al., 2014). The exact mechanical contributions of the anticlinal cell walls, consisting of two primary cells walls of neighboring cells with the middle lamella in-between, which glues adjacent pavement cells together, still remain elusive. The primary cell wall contains a network of interconnected cellulose microfibrils and a matrix composed of hemicelluloses, pectins and structural proteins, while the middle lamella primarily contains pectins (Cosgrove, 2005, 2014). The exact contribution of these different components in determining mechanical properties and final cell shape is the subject of many debates (Bidhendi and Geitmann, 2016; Cosgrove, 2016). Cellulose microfibrils are the stiffest and the most inert component of the primary cell wall and are thus thought to play a load-bearing role: their orientation creates mechanical anisotropy in the wall, which in turn restricts cell expansion in the microfibril direction (Baskin, 2005; Cosgrove, 2005, 2014, 2016; Geitmann and Ortega, 2009; Probine, Preston, 1962). The matrix, which is a dynamic component of cell walls, determines their overall mechanical behavior *via* its properties and interactions with cellulose microfibrils (Chanliaud et al., 2002; Fang and Catchmark, 2015; McCartney et al., 2000; Mikshina et al., 2015; Peaucelle et al., 2011; Ulvskov et al., 2005).

Since cell walls play an important role in controlling cell morphogenesis, we wanted to understand their role in generating wavy cell contours in the presence of tensile stress. To do so, we characterized pavement cell shape defects in different cell wall deficient mutants. We generated computational models of anticlinal walls in pavement cells, to show how in principle

structural wall heterogeneities can initiate wavy cell contours in the presence of tension. We then validated our model by measuring cell wall mechanical heterogeneities using atomic force microscopy and by revealing asymmetric distribution of various cell wall components by electron microscopy.

Results

Wavy cell contours depend on cell wall composition

Cell wall biosynthesis and remodeling-related mutants display a wide array of defects in *Arabidopsis thaliana* development. To quantify the impact of these mutations on the contours of the pavement cells, we studied the cell geometry of 16 selected mutants (Figure 1A). The interdigitated shape of the pavement cells was quantitatively analyzed by measuring the anticlinal cell wall outlines, using a semi-automated method (Figure S1A). As expected, cell areas varied among the wild type and different cell wall mutants (Figure S1D), which might influence the measurement of cell circularity and lobing of the pavement cells. Thus, we selected mutant cells whose area was similar to fully developed cells in the wild type for analysis of circularity and lobe number (Figure S1E; Figure 1B,C). Strikingly, the pavement cells of many analyzed cell wall defective mutants such as *gal10-1, mur3-1, xxt1/xxt2, xxt1/xxt2/xxt5, kor1-1* and *qua1-1* displayed cell geometry defects with increased circularity, which corresponded to decreased interdigitation. We also noticed that the *mur1-2* mutant displayed an increase in lobe number, which did not influence the circularity of its pavement cells. Moreover, the *35S::GALS-YFP* line showed a decrease in pavement cell circularity, without affecting lobe number, which suggests a positive effect of galactan on lobe formation (Figure 1B, C). Altogether, this analysis demonstrates that the formation of interdigitation in pavement cells involves an active contribution of cell wall remodeling and synthesis.

Wall-like materials bend independently of a buckling process

Early in their development, epidermal pavement cells are isodiametric and display straight cell walls, before forming wavy contours later on (e.g. Fu et al., 2002). We used a computational approach to address whether lobe formation requires local heterogeneous mechanical properties established earlier in initially straight anticlinal cell wall segments of epidermal pavement cells. Mechanical buckling is known to bend thin geometrical structures under compressive forces and

this phenomenon is also reported to occur in plant tissues (Dumais, 2007; Green, 1999; Shipman and Newell, 2004). To understand whether buckling might cause pavement cell interdigitation, we tested the influence of compression and tension on the bending process in cell walls with and without heterogeneous mechanical properties. To do so, we introduced a finite element methods (FEM) model implementing material inhomogeneity of initially straight sections, which bend under compressive or tensional loads. We demonstrated that buckling leads to bending of homogeneous wall-like structures and requires compressive forces (Figure 2A). Then we introduced local wall inhomogeneities composed of elastically stronger and weaker layers, whose order in consecutive sections was switched alternately along and across the wall. Compressive forces in the presence of inhomogeneities produced bending with the elastically stronger layer on the convex side. The direction of the deformation was reversed in the adjacent section, where the layer order was switched (Figure 2B). Next we tested the influence of tensional forces on bending behavior of homogeneous and heterogeneous walls. Homogeneous walls did not bend under tensional forces (Figure 2C). In the case of heterogeneous walls, bending was present, but the direction of the bending was altered in comparison to compressive loads. This time the elastically stronger layer was on the concave side (Figure 2D). Therefore, these simulations indicate that the tensional forces previously described in the *Arabidopsis* leaf (Sampathkumar et al., 2014) and implemented in our model (Figure 2D) can cause a bending of anticlinal cell walls, in a different manner than the compression driven buckling process (Figure 2B) and presents a possible mechanism explaining the bending of heterogeneous cell wall under tensional forces.

Dual heterogeneity of anticlinal cell walls generates bending under tensional forces

To integrate the role of anticlinal wall mechanical heterogeneities in the generation of interdigitation under tension, we built a finite element model of complete cell anticlinal walls. Since tensional forces act on the organ level (Sampathkumar et al., 2014), we assumed symmetry boundary conditions, which allowed us to treat a single cell simulation as a part of larger multicellular model. During bending under tension, the tension comes from both sides of the composite wall, which however extend to a different degree despite being under the same tensional force. This might be a topological consequence of accommodating juxtaposed cell walls that extend to different lengths when their elastic deformation reaches equilibrium. To

illustrate the precise differences in the elasticity of composite wall sections, we used a linear elastic material model. The model geometry consisted of an initially square shaped "cell" containing anticlinal walls subjected to stretching loads, as described in turgid tissues (Sampathkumar et al., 2014) (Figure 2E-G). First, we analyzed the deformation of the walls containing homogenous mechanical properties (Figure 2E) and did not observe any change in wall curvature. Next, we built a model of walls containing alternating sections of elastically stronger and weaker material along the wall (Figure 2F) and still did not detect any bending. We then introduced composite walls, built from two layers of material with different elasticity across the wall section and only a slight bending of the wall was observed (Figure 2H). Finally, heterogeneity of the cell wall mechanical properties along and across the cell wall with stronger material alternated between the inner and outer sides of each cell wall was analyzed. Such a heterogeneous composition led to a waving curvature in the walls (Figure 2G). Moreover, we demonstrated that the period and amplitude of the "lobes" were dependent on the size of the local cell wall mechanical heterogeneities (Figure 2G). This suggests that the heterogeneous material composition along and across anticlinal cell walls might actively participate in puzzle-like cell shape acquisition. Overall, these simulations indicate that mechanical heterogeneity across the cell wall thickness, present in alternating segments along the cell wall, can be sufficient to initiate the interdigitated shape of pavement cells in an epidermis under tension. To demonstrate how the elastic modulus of specified wall zones influences bending capacity of the wall, we analyzed in more detail the single wall segment of the composite wall with alternated order of elastically weaker and stronger material. We tested the effect of elasticity differences (10% and 20%) while varying the elastic modulus and observed that the deformation decreased with increasing elastic modulus values (Figure 2I). The bending deformation increased with increasing relative elasticity difference between the parts (Figure 2J). Thus we conclude that lowering the elastic modulus favors the bending behavior of the wall. Additional simulations demonstrated that the turgor pressure did not have an essential role in the lobing process (Figure 2K, L).

Differences in mechanical properties along the cell wall perimeter revealed by AFM

Because neighboring pavement cells display alternating geometrical patterns formed by lobe and neck regions, the connecting anticlinal walls shift from a curved to a straight conformation.

Moreover, within the curved zone of the cell walls, the concave side (facing the lobe of the cell) and the convex side (facing the neck of the neighboring cell) can be defined (Figure 3A). To test the importance of the cell wall within cell shape determination, we first analyzed the mechanical properties of the contiguous anticlinal walls at a subcellular resolution by using atomic force microscopy (AFM) on ultrathin paradermal sections of fully developed epidermal cells from *Arabidopsis* third leaf. In order to access anticlinal cell walls, the sections were fixed and embedded in resin, which inevitably modified the native mechanical properties of cell walls. However, such a treatment performed at a tissue scale does not change relative stiffness within a sample, as shown in other studies (Matsko and Mueller, 2004). AFM images were taken and used to quantify the stiffness within the regions of interest (ROIs) as depicted in Figures 3 and S2. ROIs were placed consecutively along and across the cell walls as depicted in Figures 3B and S2A. The stiffness was measured at multiple points in each ROI (Figures 3C, D and S2B, C). Detailed analysis of stiffness measurements for two ROIs is presented in Figures 3E-G and S2D-F. Remarkably, the mechanical properties of the cell walls were found to be heterogeneous along the perimeter of the pavement cells in wild type leaves (Figure 4A-C, Figure 4L and Table S1A). This heterogeneity could be correlated to cell wall shape: the straight regions of the anticlinal cell walls were softer than the adjacent curved regions (Figure 4B, C, L, and Table S1A). To validate the correlation between wall stiffness heterogeneity and cell wall shape, we next analyzed a mutant in which the interdigitation pattern is abolished. Here we used the constitutively active *rop2* (*CA-rop2*) mutant line in which interdigitation is almost absent (Fu et al., 2002; Li et al., 2001). AFM analysis revealed that the mechanical properties of straight anticlinal cell walls in fully developed epidermal pavement cells of the *CA-rop2* mutant were significantly more homogenous than those of the wild type (Figure 4D-F, Figure 4L, Table S1B). Note that the measurements are relative and dependent on individual samples. However, the alternating stiffness pattern was constant along the cell perimeter in different samples (Table S1A). Thus, heterogeneities in cell wall properties along the cell perimeter are correlated to the presence of wavy cell contours.

Heterogeneities in mechanical properties across the cell wall
Next, high-resolution AFM analyses were performed on ultrathin paradermal sections across cell walls in fully developed epidermal pavement cells. A detailed examination of mechanical

properties across the wall was performed by quantifying the stiffness within the concave or convex cell wall zones (see Figure 3 and Figure S2 for the method). The distribution of force measurements correlated with their localization within the cell wall in different ROIs shown in Figures 3B and S2A, revealing a stiffness gradient across the contiguous cell wall of the wild type, with the concave side being stiffer than the contiguous convex side (Figure 4G, I, L and Table S1C). However, a stiffness gradient could also be detected across the straight region (Figure 4H, I, L and Table S1D). Interestingly, only minor mechanical heterogeneities were detected across the cell walls in fully developed pavement cells of the *CA-rop2* mutant with straight anticlinal cell walls (Figure 4J-L and, Table S1E). Overall, these data are consistent with our model's assumption: contiguous walls between adjacent cells display alternating mechanical heterogeneities both along their wall perimeter and across their wall width in cells producing curved walls under tension (Figure 2D, G), while this was not the case for the *CA-rop2* mutant with straight walls (Figure 2C, E). Note that the measurements are relative and dependent on individual samples and the differences in stiffness vary between different samples (Table S1C-E). Such variability might be related to the stage of the pavement cells' development or different ages of neighboring cells influencing the cell walls' stiffness and their capacity to bend. However, the alternating stiffness detected across the cell walls in the wild type was constant in different samples. To confirm that such mechanical gradients are specific to contiguous walls that lobe, we analyzed forces across the anticlinal cell walls of non-lobing root atrichoblast cells (Figure S3A-C), in different ROIs shown in Figure S3D. In agreement with our model's assumption, only minor mechanical heterogeneities were found across these straight anticlinal cell walls, which seemed randomly distributed (Figure S3E-H).

Polar distribution of galactan and arabinan pectin components

Mechanical heterogeneities were detected along and across the anticlinal cell walls in fully developed interdigitated epidermal pavement cells of the wild type (Figure 4). Given the mechanical heterogeneities, similar inhomogeneity might also be present in the cell wall component distributions. To investigate the subparietal distribution of different primary cell wall components, we performed immunocytochemistry on ultrathin sections and analyzed the localization of various epitopes of matrix polysaccharides and cellulose *via* transmission electron microscopy (TEM) in *Arabidopsis* wild type and *CA-rop2* mutant third leaf pavement cells (Key

Resource Table). In order to maximize the efficiency and scale of the analysis, we generated an automated quantitative method for gold particle detection (Figure S4). This allowed us to determine the distribution of the epitopes within the different cell wall regions (Figure 5 and Figure S5).

While some of the analyzed epitopes were homogenously distributed across the cell wall (Figure S5), low methylesterified homogalacturonan epitopes (detected by the JIM5 antibody) were present near the middle lamella, both in the wild type and the *CA-rop2* mutant (Figure 5A-F). High methylesterified homogalacturonan epitopes (detected by JIM7) were similarly distributed in the wild type (Figure 5G-J) and they were less abundant and homogenously distributed in *CA-rop2* (Figure 5K, L). Among seven different wall epitopes we tested (Key Resource Table), two displayed a distinct polar localization across the curved part of the wall in the wild type: (1,4)-β-D-galactan epitopes (detected by LM5 antibody) and (1,5)-α-L-arabinan (detected by LM6) were mainly localized at the convex (neck) side of the cell wall and rarely observed on the concave (lobe) side (Figure 5M, N, S, T). (1,4)-β-D-galactan epitopes were also heterogeneously distributed across the straight cell wall in the wild type and in *CA-rop2* mutant, being preferentially present in close proximity to both plasma membranes (Figure 5O-R), while the density of these epitopes was lower in the mutant in comparison to the wild type. Epitopes of (1,5)-α-L-arabinan also displayed heterogeneous distribution across the straight regions, but unlike the (1,4)-β-D-galactan epitopes, they were more concentrated near the middle lamella in the wild type (Figure 5U, V), and were homogenously distributed in straight regions of cell wall in the *CA-rop2* mutant (Figure 5W, X). Intriguingly, the crystalline cellulose epitopes themselves were homogenously distributed (Figure S5M-R), indicating that their repartition *per se* is not essential for the lobing process, but their orientation and degree of interaction with other cell wall components might be. This is however technically difficult to assess. Density analysis of gold particles within straight and curved cell wall regions in wild type revealed higher density of (1,4)-β-D-galactan epitopes in the straight cell wall zones (Figure 5Y).

Note that similar heterogeneities in cell wall component distribution could be detected in another species: we analyzed the epidermis in camphor tree (*Cinnamonum camphora*), an early diverging angiosperm plant. Both (1,4)-β-D-galactan and (1,5)-α-L-arabinan epitopes displayed a similar polar localization in the curved regions (Figure S6A, C) but not in the straight parts of the cell walls (Figure S6B, D), while fucosylated xyloglucan epitopes were distributed uniformly in the

curved and straight zones of the cell wall (Figure S6E, F). Altogether, these results are consistent with the presence a mechano-chemical asymmetry across the cell wall of wavy pavement cells in plants.

Mechano-chemical polarization of anticlinal cell walls appears before lobe formation

So far, our results are consistent with a model in which jigsaw puzzle cell shapes require mechanical and structural heterogeneities along and across anticlinal walls. Yet, our model infers that such heterogeneities should also precede lobing. To test that prediction, we analyzed cell wall mechano-chemical properties before bending occurs. In young leaves, the presence of meristemoids with stereotypical cell division patterns (Robinson et al., 2011) and cell shapes provides the opportunity to predict the position of a wall bending event before it occurs (Figure 6A). At such positions, we analyzed the mechanical properties along and across the straight or early bending cell walls in the wild type. Remarkably, before wall bending was visible, a mechanical heterogeneity was detected along the anticlinal wall in the wild type, being softer in the middle part where the lobe will develop in the future and stiffer on the two sides closer to the corners (Figure 6A-F). This suggests that the initiation of the lobing process might require a local softening of the cell wall. These data are in direct correlation with our *in silico* prediction showing that the bending deformation occurs more easily for softer wall zones (Figure 2I). By quantifying the stiffness on each side of cell walls that are yet to lobe (Figure 6G-M), heterogeneous mechanical properties were also found to be present across straight or early bending cell walls, being stiffer at the future concave side (younger cell side) and softer in the future convex side (older cell side) of the wall in the wild type (Figure 6M). Our hypothesis is that the stiffness gradient precedes lobing, being already present across straight cell walls while deformation is not yet visible. However, the range of stiffness needed to initiate the bending process remains difficult to address and cannot be resolved using methods analyzing only a single time point.

To further explore whether the structural heterogeneities are also generated before lobing occurs, immunogold labelling was performed on straight cell walls of the wild type and *CA-rop2* mutant at this early developmental stage. In wild type, the occurrence of galactan, arabinan and low methylesterified homogalacturonan epitopes varied along the perimeter of the straight cell walls, being significantly more abundant in the middle cell wall zone where bending will develop and

form a curved wall, while fucosylated xyloglucan was less abundant in this zone (Figure 7 and S7). In contrast, the *CA-rop2* mutant had less galactan, arabinan, low methylesterified homogalacturonan and fucosylated xyloglucan signals in the middle zones than in the corner regions of cell walls (Figure 7 and S7). The narrow width of the cell walls made the investigation of the epitopes' relative distributions across the walls unfeasible.

Observations in the wild type indicate that mechanical heterogeneities are present along cell walls, being softer in the middle part where the lobe will develop, and these differences also occur across straight walls between younger and older cells before the lobing process is initiated. Our results also demonstrate that anticlinal cell walls modify their composition along their perimeter in a strikingly different way in the wild type and *CA-rop2* mutant, showing that wavy cell contours involve extensive control of wall mechano-chemical asymmetries.

Discussion

By analyzing mutants with a wide range of defects related to major cell wall components, we first showed that even minor alterations in the cell wall composition lead to severe defects in the geometry of the leaf pavement cells. A computational modeling approach suggested that mechanical heterogeneity along and across the anticlinal cell wall is needed to initiate the interdigitated shape of pavement cells in an epidermis that is under tension. Such heterogeneities were detected by AFM in straight cell walls prior to and at a very early stage of lobe formation. In addition, the direction of bending from the mechanically stronger towards the mechanically weaker cell wall domain, as predicted by the model, was confirmed by AFM in anticlinal walls at the very early stage of wall lobing. We detected lower elastic modulus in the cell wall side facing the younger cell prior to lobe formation, which corresponds to the future concave side. Moreover, these heterogeneous mechanical properties were related to differential distribution of specific components such as low methylesterified homogalacturonan, $(1,4)$-β-D-galactan and $(1,5)$-α-L-arabinan, suggesting that these components could actively modulate wall elasticity and pointing to these epitopes as contributing to the observed cell wall weakening. Furthermore, we demonstrated that mechanical heterogeneities as well as altered distributions of cell wall components precede wall bending. Observations in older leaves, where the lobes were already present, also demonstrated a correlation between the abundance of $(1,4)$-β-D-galactan and $(1,5)$-α-L-arabinan at the mechanically weaker concave sites at the lobes, as well as at the

mechanically weaker straight wall segments, where cell wall expansion likely continues after lobe emergence.

It is well-known that pectins have an impact on the mechanics of the cell wall (Dick-Pérez et al., 2011; Dyson et al., 2012; Park and Cosgrove, 2012; Peaucelle et al., 2011, 2015) and cell wall stiffness likely depends on the relation between pectin and cellulose, cellulose/pectin composites being strongly influenced by pectin conformation (Agoda-Tandjawa et al., 2012). Recently, pectin-derived mechanical heterogeneities were found to underlie polar (Palin and Geitmann, 2012) and anisotropic growth (Peaucelle et al., 2015). Mechanistically, it remains to investigate if and how pectins trigger the observed mechanical heterogeneities. Our results show that straight cell walls display local weakening on the future lobe side, which corresponds to increased concentration of low methylesterified homogalacturonan, (1,4)-β-D-galactan and (1,5)-α-L-arabinan epitopes. Homogalacturonan methylesterification level and pattern are thought to also play a role in regulating cell wall properties, notably by formation of calcium-mediated crosslinks (resulting in stiffer walls) (Derbyshire et al., 2007; Ross et al., 2011; Siedlecka et al., 2007) and by determining sites and pH environment for homogalacturonan degradation (resulting in softer walls) (Ha et al., 2005; Jarvis, 1992; Parre and Geitmann, 2005). Accumulation of (1,4)-β-D-galactan epitopes near the necks could be explained by several factors. First, galactan epitopes are enriched at the proximity of the plasma membrane where new wall material is deposited. Moreover, tensile stresses are thought to be highest in the peripheral cell wall regions under strain (McCartney et al., 2000), suggesting that such asymmetric distribution may depend on stress levels across cell walls. In particular, we found that (1,4)-β-D-galactans are associated with decreased mechanical stiffness; arguably, this could be due to their water retaining viscoelastic character (Ha et al., 2005; McCartney et al., 2000). Galactan and arabinan display high dynamicity and modulate primary cell wall microenvironments (Ulvskov et al., 2005) during hydrous fluctuations and fast cell wall deformations (Ha et al., 2005; MacDougall et al., 1997; Ryden et al., 2000). Cell wall bending in pavement cells may very well be consistent with such local environments.

Altogether, our model and data show that the dynamics and hybrid mechano-chemical nature of plant walls might contribute to generating wavy cell contours in the absence of compression. Our results also prove that contiguous cells retain a large level of control over their cell walls, adding another layer of complexity to their mechanics and chemistry. Because such mechano-chemical

polarity likely exists in other tissues, this finding may very well have fundamental implications for cell polarity in plants in general.

Author Contributions

M.M., B.Z.M., E.M. and S.R. initiated the work. M.M., P.G., E.M. and S.R. designed the experiments. M.M. carried out most of the biological experiments. I.M.S designed the software for automated gold particle detection and performed the quantification analysis with the assistance of M.M. T.V. developed the confocal image data analysis. P.G. acquired confocal images and performed their analysis with the assistance of T.V. H.J. and P.K. performed the computational model. P.G. O.H. and P.M. assisted M.M. in the AFM analysis. P.G. and C.V. assisted M.M. in the EM analysis. M.M., P.G. and S.R. wrote the manuscript. All authors revised the manuscript.

References

Agoda-Tandjawa, G., Durand, S., Gaillard, C., Garnier, C., and Doublier, J.L. (2012). Properties

of cellulose/pectins composites: implication for structural and mechanical properties of cell wall. Carbohydr. Polym. *90*, 1081–1091.

Armour, W.J., Barton, D. a, Law, a M., and Overall, R.L. (2015). Differential Growth in Periclinal and Anticlinal Walls during Lobe Formation in Arabidopsis Cotyledon Pavement Cells. Plant Cell *27*, 2484–2500.

Bai, Y., Falk, S., Schnittger, A., Jakoby, M.J., and Hülskamp, M. (2010). Tissue layer specific regulation of leaf length and width in Arabidopsis as revealed by the cell autonomous action of ANGUSTIFOLIA. Plant J. *61*, 191–199.

Baskin, T.I. (2005). Anisotropic Expansion of the Plant Cell Wall. Annu. Rev. Cell Dev. Biol. *21*, 203–222.

Bidhendi, A.J., and Geitmann, A. (2016). Relating the mechanics of the primary plant cell wall to morphogenesis. J. Exp. Bot. *67*, 449–461.

Bonin, C.P., Potter, I., Vanzin, G.F., and Reiter, W.D. (1997). The MUR1 gene of Arabidopsis thaliana encodes an isoform of GDP-D-mannose-4,6-dehydratase, catalyzing the first step in the de novo synthesis of GDP-L-fucose. Proc. Natl. Acad. Sci. U. S. A. *94*, 2085–2090.

Bouton, S., Leboeuf, E., Mouille, G., Leydecker, M.-T., Talbotec, J., Granier, F., Lahaye, M., Höfte, H., and Truong, H.-N. (2002). QUASIMODO1 encodes a putative membrane-bound glycosyltransferase required for normal pectin synthesis and cell adhesion in Arabidopsis. Plant Cell *14*, 2577–2590.

Cavalier, D.M., Lerouxel, O., Neumetzler, L., Yamauchi, K., Reinecke, A., Freshour, G., Zabotina, O.A., Hahn, M.G., Burgert, I., Pauly, M., et al. (2008). Disrupting Two Arabidopsis thaliana Xylosyltransferase Genes Results in Plants Deficient in Xyloglucan, a Major Primary Cell Wall Component. Plant Cell Online *20*, 1519–1537.

Chanliaud, E., Burrows, K.M., Jeronimidis, G., and Gidley, M.J. (2002). Mechanical properties of primary plant cell wall analogues. Planta *215*, 989–996.

Chen, X.-Y., Liu, L., Lee, E., Han, X., Rim, Y., Chu, H., Kim, S.-W., Sack, F., and Kim, J.-Y. (2009). The Arabidopsis callose synthase gene GSL8 is required for cytokinesis and cell patterning. Plant Physiol. *150*, 105–113.

Cosgrove, D.J. (2005). Growth of the plant cell wall. Nat. Rev. Mol. Cell Biol. *6*, 850–861.

Cosgrove, D.J. (2014). Re-constructing our models of cellulose and primary cell wall assembly. Curr. Opin. Plant Biol. *22*, 122–131.

Cosgrove, D.J. (2016). Plant cell wall extensibility: Connecting plant cell growth with cell wall structure, mechanics, and the action of wall-modifying enzymes. J. Exp. Bot. *67*, 463–476.

Derbyshire, P., McCann, M.C., and Roberts, K. (2007). Restricted cell elongation in Arabidopsis hypocotyls is associated with a reduced average pectin esterification level. BMC Plant Biol. *7*, 31.

Derjaguin, B. V, Muller, V.M., and Toporov, Y.. (1975). Effect of contact deformations on the adhesion of particles. J. Colloid Interface Sci. *53*, 314–326.

Desnos, T., Orbović, V., Bellini, C., Kronenberger, J., Caboche, M., Traas, J., and Höfte, H. (1996). Procuste1 mutants identify two distinct genetic pathways controlling hypocotyl cell elongation, respectively in dark- and light-grown Arabidopsis seedlings. Development *122*, 683–693.

Dick-Pérez, M., Zhang, Y., Hayes, J., Salazar, A., Zabotina, O. a., and Hong, M. (2011). Structure and interactions of plant cell-wall polysaccharides by two- and three-dimensional magic-angle-spinning solid-state NMR. Biochemistry *50*, 989–1000.

Dumais, J. (2007). Can mechanics control pattern formation in plants? Curr. Opin. Plant Biol. *10*, 58–62.

Dyson, R.J., Band, L.R., and Jensen, O.E. (2012). A model of crosslink kinetics in the expanding plant cell wall: Yield stress and enzyme action. J. Theor. Biol. *307*, 125–136.

Dyson, R.J., Vizcay-Barrena, G., Band, L.R., Fernandes, A.N., French, A.P., Fozard, J.A., Hodgman, T.C., Kenobi, K., Pridmore, T.P., Stout, M., et al. (2014). Mechanical modelling quantifies the functional importance of outer tissue layers during root elongation and bending. New Phytol. *202*, 1212–1222.

Elsner, J., Michalski, M., and Kwiatkowska, D. (2012). Spatiotemporal variation of leaf epidermal cell growth: A quantitative analysis of Arabidopsis thaliana wild-type and triple cyclinD3 mutant plants. Ann. Bot. *109*, 897–910.

Fang, L., and Catchmark, J.M. (2015). Characterization of cellulose and other exopolysaccharides produced from Gluconacetobacter strains. Carbohydr. Polym. *115*, 663–669.

Fu, Y., Li, H., and Yang, Z. (2002). The ROP2 GTPase controls the formation of cortical fine F-actin and the early phase of directional cell expansion during Arabidopsis organogenesis. Plant Cell *14*, 777–794.

Fu, Y., Gu, Y., Zheng, Z., Wasteneys, G., and Yang, Z. (2005). Arabidopsis interdigitating cell

growth requires two antagonistic pathways with opposing action on cell morphogenesis. Cell *120*, 687–700.

Geitmann, A., and Ortega, J.K.E. (2009). Mechanics and modeling of plant cell growth. Trends Plant Sci. *14*, 467–478.

Green, P.B. (1999). Expression of pattern in plants: Combining molecular and calculus-based biophysical paradigms. Am. J. Bot. *86*, 1059–1076.

Ha, M.A., Viëtor, R.J., Jardine, G.D., Apperley, D.C., and Jarvis, M.C. (2005). Conformation and mobility of the arabinan and galactan side-chains of pectin. Phytochemistry *66*, 1817–1824.

Hayot, C.M., Forouzesh, E., Goel, A., Avramova, Z., and Turner, J.A. (2012). Viscoelastic properties of cell walls of single living plant cells determined by dynamic nanoindentation. J. Exp. Bot. *63*, 2525–2540.

Hutter, J.L., and Bechhoefer, J. (1993). Calibration of Atomic-Force Microscope Tips. Rev. Sci. Instrum. *64*, 1868–1873.

Jarvis, M.C. (1992). Control of thickness of collenchyma cell walls by pectins. Planta *187*, 218–220.

Kutschera, U., and Niklas, K.J. (2007). The epidermal-growth-control theory of stem elongation: An old and a new perspective. J. Plant Physiol. *164*, 1395–1409.

Li, H., Shen, J.J., Zheng, Z.L., Lin, Y., and Yang, Z. (2001). The Rop GTPase switch controls multiple developmental processes in Arabidopsis. Plant Physiol. *126*, 670–684.

Lin, D., Cao, L., Zhou, Z., Zhu, L., Ehrhardt, D., Yang, Z., and Fu, Y. (2013). Rho GTPase signaling activates microtubule severing to promote microtubule ordering in arabidopsis. Curr. Biol. *23*, 290–297.

Liwanag, A.J.M., Ebert, B., Verhertbruggen, Y., Rennie, E.A., Rautengarten, C., Oikawa, A., Andersen, M.C.F., Clausen, M.H., and Scheller, H. V. (2012). Pectin Biosynthesis: GALS1 in Arabidopsis thaliana Is a -1,4-Galactan -1,4-Galactosyltransferase. Plant Cell *24*, 5024–5036.

Maaloum, M. Lévy, R. (2002). Measuring the spring constant of atomic force microscope cantilevers : thermal R L ´. Nanotechnology *33*, 33–37.

MacDougall, A.J., Rigby, N.M., and Ring, S.G. (1997). Phase Separation of Plant Cell Wall Polysaccharides and Its lmplications for Cell Wall Assembly'. Plant Physiol. *114*, 353–362.

Marcotrigiano, M. (2010). A role for leaf epidermis in the control of leaf size and the rate and extent of mesophyll cell division. Am. J. Bot. *97*, 224–233.

Matsko, N., and Mueller, M. (2004). AFM of biological material embedded in epoxy resin. J. Struct. Biol. *146*, 334–343.

McCartney, L., Ormerod, A.P., Gidley, M.J., and Knox, J.P. (2000). Temporal and spatial regulation of pectic (1-4)-β-D-galactan in cell walls of developing pea cotyledons: Implications for mechanical properties. Plant J. *22*, 105–113.

Mikshina, P. V., Idiyatullin, B.Z., Petrova, A.A., Shashkov, A.S., Zuev, Y.F., and Gorshkova, T.A. (2015). Physicochemical properties of complex rhamnogalacturonan I from gelatinous cell walls of flax fibers. Carbohydr. Polym. *117*, 853–861.

Nezhad, A.S., Naghavi, M., Packirisamy, M., Bhat, R., and Geitmann, A. (2013). Quantification of the Young's modulus of the primary plant cell wall using Bending-Lab-On-Chip (BLOC). Lab Chip *13*, 2599–2608.

Nicol, F., His, I., Jauneau, A., Vernhettes, S., Canut, H., and Höfte, H. (1998). A plasma membrane-bound putative endo-1,4-β-D-glucanase is required for normal wall assembly and cell elongation in Arabidopsis. EMBO J. *17*, 5563–5576.

Palin, R., and Geitmann, A. (2012). The role of pectin in plant morphogenesis. BioSystems *109*, 397–402.

Park, Y.B., and Cosgrove, D.J. (2012). A Revised Architecture of Primary Cell Walls Based on Biomechanical Changes Induced by Substrate-Specific Endoglucanases. Plant Physiol. *158*, 1933–1943.

Parre, E., and Geitmann, A. (2005). Pectin and the role of the physical properties of the cell wall in pollen tube growth of Solanum chacoense. Planta *220*, 582–592.

Peaucelle, A., Braybrook, S.A., Le Guillou, L., Bron, E., Kuhlemeier, C., and Höfte, H. (2011). Pectin-Induced Changes in Cell Wall Mechanics Underlie Organ Initiation in Arabidopsis. Curr. Biol. *21*, 1720–1726.

Peaucelle, A., Wightman, R., and Höfte, H. (2015). The Control of Growth Symmetry Breaking in the Arabidopsis Hypocotyl. Curr. Biol. 1746–1752.

Pound, M.P., French, A.P., Wells, D.M., Bennett, M.J., and Pridmore, T.P. (2012). CellSeT: Novel Software to Extract and Analyze Structured Networks of Plant Cells from Confocal Images. Plant Cell *24*, 1353–1361.

Probine, Preston (1962). Cell growth and the structure and mechanical properties of the wall in internodal cells of Nitella opaca. J Exp Bot *13*, 111–127.

Reiter, W.D., Chapple, C., and Somerville, C.R. (1997). Mutants of Arabidopsis thaliana with altered cell wall polysaccharide composition. Plant J. *12*, 335–345.

Robinson, S., Reuille, P.B. De, Chan, J., Bergmann, D., Prusinkiewicz, P., and Coen, E.S. (2011). Generation of spatial patterns through cell polarity switching. Science (80-.). *333*, 1436–1440.

Ross, H.A., Morris, W.L., Ducreux, L.J.M., Hancock, R.D., Verrall, S.R., Morris, J.A., Tucker, G.A., Stewart, D., Hedley, P.E., Mcdougall, G.J., et al. (2011). Pectin engineering to modify product quality in potato. Plant Biotechnol. J. *9*, 848–856.

Ryden, P., MacDougall, A.J., Tibbits, C.W., and Ring, S.G. (2000). Hydration of pectic polysaccharides. Biopolymers *54*, 398–405.

Sampathkumar, A., Krupinski, P., Wightman, R., Milani, P., Berquand, A., Boudaoud, A., Hamant, O., Jönsson, H., and Meyerowitz, E.M. (2014). Subcellular and supracellular mechanical stress prescribes cytoskeleton behavior in *Arabidopsis* cotyledon pavement cells. Elife *3*, 1–20.

Sampedro, J., Gianzo, C., Iglesias, N., Guitian, E., Revilla, G., and Zarra, I. (2012). AtBGAL10 is the main xyloglucan -galactosidase in arabidopsis, and its absence results in unusual xyloglucan subunits and growth defects. Plant Physiol. *158*, 1146–1157.

Savaldi-Goldstein, S., and Chory, J. (2008). Growth coordination and the shoot epidermis. Curr. Opin. Plant Biol. *11*, 42–48.

Savaldi-Goldstein, S., Peto, C., and Chory, J. (2007). The epidermis both drives and restricts plant shoot growth. Nature *446*, 199–202.

Schindelin, J., Arganda-Carreras, I., Frise, E., Kaynig, V., Longair, M., Pietzsch, T., Preibisch, S., Rueden, C., Saalfeld, S., Schmid, B., et al. (2012). Fiji: an open source platform for biological image analysis. Nat. Methods *9*, 676–682.

Schneider, C. a, Rasband, W.S., and Eliceiri, K.W. (2012). NIH Image to ImageJ: 25 years of image analysis. Nat. Methods *9*, 671–675.

Shipman, P.D., and Newell, A.C. (2004). Phyllotactic patterns on plants. Phys. Rev. Lett. *92*, 168102–1.

Siedlecka, A., Wiklund, S., Peronne, M.-A., Micheli, F., Lesniewska, J., Sethson, I., Edlund, U., Richard, L., Sundberg, B., and Mellerowicz, E.J. (2007). Pectin Methyl Esterase Inhibits Intrusive and Symplastic Cell Growth in Developing Wood Cells of Populus. Plant Physiol. *146*,

554–565.

Swarup, R., Kramer, E.M., Perry, P., Knox, K., Leyser, H.M.O., Haseloff, J., Beemster, G.T.S., Bhalerao, R., and Bennett, M.J. (2005). Root gravitropism requires lateral root cap and epidermal cells for transport and response to a mobile auxin signal. Nat. Cell Biol. *7*, 1057–1065.

Ulvskov, P., Wium, H., Bruce, D., Jørgensen, B., Qvist, K.B., Skjøt, M., Hepworth, D., Borkhardt, B., and Sørensen, S.O. (2005). Biophysical consequences of remodeling the neutral side chains of rhamnogalacturonan I in tubers of transgenic potatoes. Planta *220*, 609–620.

Uyttewaal, M., Burian, A., Alim, K., Landrein, B., Borowska-Wykręt, D., Dedieu, A., Peaucelle, A., Ludynia, M., Traas, J., Boudaoud, A., et al. (2012). Mechanical Stress Acts via Katanin to Amplify Differences in Growth Rate between Adjacent Cells in Arabidopsis. Cell *149*, 439–451.

Zabotina, O. a., Van De Ven, W.T.G., Freshour, G., Drakakaki, G., Cavalier, D., Mouille, G., Hahn, M.G., Keegstra, K., and Raikhel, N. V. (2008). Arabidopsis XXT5 gene encodes a putative α-1,6-xylosyltransferase that is involved in xyloglucan biosynthesis. Plant J. *56*, 101–115.

Zabotina, O. a., Avci, U., Cavalier, D., Pattathil, S., Chou, Y.-H., Eberhard, S., Danhof, L., Keegstra, K., and Hahn, M.G. (2012). Mutations in Multiple XXT Genes of Arabidopsis Reveal the Complexity of Xyloglucan Biosynthesis. Plant Physiol. *159*, 1367–1384.

Zhong, R., Kays, S.J., Schroeder, B.P., and Ye, Z.-H. (2002). Mutation of a chitinase-like gene causes ectopic deposition of lignin, aberrant cell shapes, and overproduction of ethylene. Plant Cell *14*, 165–179.

Main Figure Titles and Legends

Figure 1. Cell wall composition controls pavement cell shape definition

Representative confocal microscopy images (**A**) and cell shape properties (**B, C**) of pavement cells in the 3rd leaf of two-week-old *Arabidopsis* wild types and 16 mutants deficient in a wide array of cell wall components (Key Resource Table, see Figure S1 for method). Scale bar represents 20 μm. Lobe number (**B**) and circularity (**C**) of each cell were measured in an automated way to characterize the shape of fully developed pavement cells similar in cell area to Col-0 (Figure S1). Statistics were performed using ANOVA and Tukey's test. Means ± SE are shown, n values are displayed on the graphs, $*P < 0.05$; $**P < 0.01$; $***P < 0.001$.

Figure 2. Model of epidermal anticlinal cell wall waving under tension

Fine element modeling (Key Resource Table) of initially straight segments (black frames) consisting of homogeneous (**A, C**) and heterogeneous (**B**, **D**) composites (weaker: blue, stronger: red) display different bending under compressive (**A, B**) and under tensional (**C, D**) forces (both acting along the long axis (red arrows)). The uniaxial compressive forces caused buckling of homogenous materials (bending related to the instability of the mechanical equilibrium) (**A**). Uniaxial compression of the material (consisted of two layers characterized by different elasticity) led to bending, with elastically stronger layer on the convex side (red) (**B**). While tensional uniaxial loads did not lead to bending of homogeneous walls (**C**) they did cause bending of heterogeneous composite materials (consisted of two layers displaying different elasticity), with the elastically stronger layer on the concave side (red) (**D**).

Finite element model presenting elastic deformation at equilibrium (final state of the simulation) of the anticlinal walls of the initially square "cell" (**E-G**). The black wireframe shows initial position of the walls. The red arrows show the direction of loading forces, while the opposite wall ends are fixed in the direction of the forces, effectively realizing symmetry boundary conditions. The extension of anticlinal cell walls assuming homogenous material throughout the walls - the walls under stretching loads remain straight (**E**). Material heterogeneity introduced along the walls where elastically stronger sections of material (red) are staggered with sections of weaker material (blue) - stretching deforms both section types in different proportions but the walls remain straight (**F**). The extension of anticlinal cell walls, where the order of elastically stronger (red) and weaker (blue) layers is alternated in sections along the wall length - the regions where the stronger material is on the inner side of composite cell walls bend outwards, simulating potential initiation of future lobes. The regions where the weaker material is on the inner side bend inwards into the cell, simulating potential initiation of future necks. Different sizes of local cell wall inhomogeneities along the cell wall modify lobe amplitude. The anticlinal walls were built of staggered regions of elastically stronger (red) and weaker (blue) material. The number of staggered sections varied in each wall from 4 to 7 (**G**). Different mechanical properties across the cell wall width (cell wall consisted of elastically weaker (blue) and stronger (red) segments) led to bending deformation under tensional forces (**H**). Graph presenting the relation between the bending deformation and elastic modulus for 10% (blue line) and 20% (red line) differences in the mechanical properties across the walls (absolute stiffness values are

changed from 50kPa (40kPa for weak part) to 500kPa (400kPa for weak part)) (**I**). Graph presenting the relation between bending deformation and relative elasticity difference (from 0 to 60%). The elasticity of the hard part was kept constant at 100 kPa (**J**). Effect of turgor pressure on the curving of the wall (**K, L**). Behavior of heterogeneous wall segments without (**K**) and with (**L**) application of 1 MPa turgor pressure acting on both sides of the wall. The turgor pressure did not affect the bending but did have a slight effect of compressing the wall, particularly visible for the weak part of the material (red).

Figure 3. Quantification method for stiffness analysis across the cell wall

Drawing illustrating different cell wall regions measured along: curved (yellow) and straight (white) and across: convex (x) and concave (e) cell wall regions (**A**). AFM image taken as a representative example to explain in detail how the forces were quantified (Key Resource Table) (stiffer places with higher apparent elastic modulus Ea are brighter). The white rectangles indicate different ROIs (regions of interest) quantified in convex (x) and concave (e) regions along the cell walls (positions 1-18) (the same image as in Figure 4G) (**B**). Table presenting stiffness measurement averages, standard errors (SE), and number of samples (n) at different ROIs shown in B (**C**). Graph presenting stiffness in convex (x) and concave (e) regions along the walls (1-18) measured in different ROIs shown in B (**D**). AFM image presenting the cell wall stiffness with indicated convex and concave regions (used to extract force curves for F and G). The number of quantification points were n=184 for the convex side and n=207 for the concave side (**E**). Distribution of stiffness measured in convex and concave cell wall regions depicted in E (**F**). Graph presenting the normal distribution of stiffness measured between convex and concave cell wall regions depicted in E (**G**).

Figure 4. Mechanical properties are heterogeneous across the wall and along its perimeter

Representative AFM images of anticlinal pavement cell walls in the wild type (**A**) and at higher resolution (**B**). White square in A represents magnification shown in B. AFM images of *CA-rop2* mutant (**D**) and at higher resolution (**E**). White square in D represents magnification shown in E. Graphic representation of stiffness (apparent elastic modulus Ea) quantification along straight and curved parts of the cell walls in wild type depicted in B (**C**) and along straight cell walls in *CA-rop2* mutant depicted in E (**F**). The numbers (**F**) correspond to the measured positions

depicted in E. Representative high resolution AFM images of anticlinal pavement cell walls of the wild type in the curved (**G**) and straight (**H**) zones. Graphic representation of stiffness quantification across the curved and straight cell walls in the wild type depicted in G, H (**I**). Representative high resolution AFM image of straight cell walls in *CA-rop2* mutant (**J**). Graphic representation of stiffness quantification across the straight cell walls in *CA-rop2* mutant depicted in J (**K**). The letters A and B (H-K) correspond to sides of the cell wall where stiffness was measured. Measured forces were significantly different between various cell wall zones in the wild type and in *CA-rop2*. Table presenting the average stiffness differences detected between various cell wall regions (see indicated frequencies), standard errors (SE), frequency of curved or concave cell wall regions being stiffer (f) and total number of AFM images measured (n) (see Table S1 presenting the values of individual samples) (**L**). Error bars correspond to ± SE. Statistical significance tested by Student's T-test, (p-value: ***$P < 0.001$). In the AFM images, stiffer places with higher apparent elastic modulus Ea are brighter.

Figure 5. Distribution of low and high methylesterified homogalacturonans, (1,4)-β-D-galactans and (1,5)-α-L-arabinans in pavement cell walls

Immunogold labelling of cell wall epitopes in pavement cells in the wild type (**A-D**, **G-J, M-P, S-V**) and in the *CA-rop2* mutant (**E**, **F**, **K**, **L**, **Q**, **R**, **W**, **X**) (Key Resource Table). Representative TEM images and graphs presenting the distribution of low methylesterified homogalacturonan epitopes (JIM5) and high methylesterified homogalacturonan epitopes (JIM7), in curved (**A-B** and **G-H**, respectively) and straight (**C-D** and **I- J**, respectively) cell walls in wild type and straight cell walls in the *CA-rop2* mutant (**E-F** and **K-L**, respectively). Number of images analyzed: B=24; D=48; F=15; H=31; J=55; L=24. Representative TEM images presenting polar distribution of (1,4)-β-D-galactan (LM5) epitopes at the convex side in curved cell walls in the wild type (**M**) and their distribution close to the plasma membranes in straight cell walls in the wild type (**O**) and in straight cell walls in the *CA-rop2* mutant (**Q**). Representative images presenting distribution of (1,5)-α-L-arabinan (LM6) epitopes in curved (**S**) and in straight (**U**) cell walls in the wild type and homogenous distribution in straight cell walls of the *CA-rop2* mutant (**W**). Statistical quantification of gold particle distribution across the cell wall in different cell wall regions (in the curved parts: convex, middle and concave, in the straight parts: close to the plasma membranes (PM) and in the middle): distribution of LM5 recognized epitopes in

curved (**N**) and straight (**P**) cell wall zones in the wild type and straight cell walls in *CA-rop2* mutant (**R**). Distribution of LM6 recognized epitopes in curved (**T**) and straight (**V**) cell wall zones in the wild type and straight cell walls in *CA-rop2* mutant (**X**). Values in B, D, F, H, J, L, N, P, R, T, V, X represent % of gold particle counts in different zones, sum of all zones = 100%. Number of images analyzed: N=55; P=56; R=28; T=50; V=59; X=16. Scale bar represents 0.5 µm. Indicated quantifications of gold particle distribution were significantly different between different cell wall zones in the wild type and in *CA-rop2*. Density of different cell wall epitopes between curved and straight cell wall zones in the wild type (**Y**). Error bars correspond to ± SE. Statistical significance tested by Student's T-test, *$P < 0.05$; **$P < 0.01$; ***$P < 0.001$).

Figure 6. Mechanical properties of non-lobed cells

Representative AFM image of anticlinal pavement cell walls in expanding epidermis of young leaves in wild type (white rectangles indicate quantified cell walls) (**A**). White squares in A represent magnifications shown in B and D. AFM images of the cell walls in the wild type at higher resolution (**B**, **D**). White square in D represents magnification shown in F. Graphic representation of stiffness (apparent elastic modulus Ea) quantification along cell walls depicted in B (**C**). Graphic representation of stiffness quantified along cell walls in the wild type depicted in D (**E**). High resolution image taken as a representative example to explain in detail how the forces were quantified across the cell walls (same sample as image in D) (**F, G**). White square in F represents magnification shown in G. The white rectangles indicate ROIs (regions of interest) quantified on two sides (A and B) along the cell walls (positions 1-9) (**G**). Table presenting averages, standard errors (SE), and number of quantification points (n) for stiffness measured in different ROIs shown in G (**H**). Graph presenting stiffness on two sides (A and B) along the cell walls (positions 1-9) measured in different ROIs shown in G (**I**). AFM image with black rectangles indicating the position where samples were taken in zone A (n=182) and in zone B (n=169) (**J**), used to quantify stiffness for K and L. Graph presenting the distribution of stiffness measured in convex and concave cell wall regions depicted in J (**K**). Graph presenting the normal distribution of stiffness measured between two cell wall regions depicted in J (**L**). Graph presenting the stiffness measured on two sides (A and B) of the walls depicted in J (**M**). Indicated measured forces were significantly different between various cell wall zones in the wild type. Error bars correspond to ± SE. Statistical significance tested by a T-test, (p-value: *P

< 0.05; ***$P < 0.001$). In the AFM images, stiffer places with higher apparent elastic modulus Ea are brighter.

Figure 7. Distribution of matrix polysaccharides along straight cell walls

Representative TEM images presenting distribution of (1,4)-β-D-galactan epitopes (LM5) in the wild type (**A**) and in the *CA-rop2* mutant (**B**). Statistical quantification of gold particle distribution along the straight cell walls in the wild type (**C**) and in the *CA-rop2* mutant (**D**). Values represent % of gold particles in different cell wall subdomains, all gold particles counted = 100%. Number of images analyzed: C=20; D=24. Scale bar = 0.5 μm. Indicated quantifications of gold particle distribution showed significantly increased number of gold particles in the middle zone of the cell wall in the wild type. Error bars correspond to ± SE. Statistical significance tested by Student's T-test (*$P < 0.05$; ***$P < 0.001$).

STAR Methods

CONTACT FOR REAGENT AND RESOURCE SHARING

Further information and requests for resources and reagents should be directed to and will be fulfilled by the Lead Contact, Stephanie Robert (Stephanie.Robert@slu.se).

EXPERIMENTAL MODEL AND SUBJECT DETAILS

*Arabidopsis thaliana***:** Before sowing, *Arabidopsis thaliana* seeds were sterilized (2 mins in 70% EtOH with Tween20, replaced with 95% EtOH and left until dry) and stratified at 4°C for 48 h for uniform germination. Seedlings were grown for 14 days at 22°C with 16 h of light per day on vertical plates of growth medium containing 1/2MS and 1% sucrose (Fisher) at pH 5.6 with 0.7% agar (Duchefa Biochemie). Epidermal pavement cells were analyzed on the adaxial side of the 3rd leaf (in order of appearance: cotyledons, leaf 1, leaf 2, leaf 3), which were 6-8 mm long and 4-5 mm wide, from 14-day-old *Arabidopsis* plants as described in (Fu et al., 2002). For analysis of non-lobed pavement cell in the wild type, the 5th leaf from 14-day-old *Arabidopsis* plants was used. The *CA-rop2* mutant line (Fu et al., 2002) was used in AFM and EM experiments. The pavement cell screen was performed on *Arabidopsis* lines: *gal10-1* (Sampedro

et al., 2012); *gals1*, *35S::GALS-YFP* (Liwanag et al., 2012); *gsl8-2* (Chen et al., 2009); *kor1-1* (Nicol et al., 1998); *mur1-2* (Bonin et al., 1997); *mur2-1* (Reiter et al., 1997); *mur3-1* (Reiter et al., 1997); *mur4-1* (Reiter et al., 1997); *pom1-2* (Zhong et al., 2002); *prc1-1* (Desnos et al., 1996); *qua1-1*, *qua2-1* (Bouton et al., 2002); *xxt1/xxt2* (Cavalier et al., 2008); *xxt5* (Zabotina et al., 2008); *xxt1/xxt2/xxt5* (Zabotina et al., 2012). Columbia (Col-0) ecotype was used as wild-type control in seedling growth experiments, except for *kor1-1* and *qua1-1* (Wassilewskija (WS) ecotype) (Key Resource Table).

Cinnamonum camphora: Five-year-old camphor trees (*Cinnamomum camphora*, Lauraceae family) were cultivated in a greenhouse with non-controlled temperature and lighting. Fully developed leaves were collected from five different trees. Epidermal pavement cells were analyzed on the adaxial side of the leaf.

METHOD DETAILS

Atomic Force Microscopy

AFM indentation experiments were carried out with a Catalyst Bioscope (Bruker Nano Surface, Santa Barbara, CA), that was mounted on an optical macroscope (MacroFluo, Leica) using the objectives 5x and 20x (Plano objective, Leica). To create an elastic modulus map, PeakForce Quantitative Nanoscale Mechanical Characterization (QNM) AFM mode was used (Foster, 2012). A Nanoscope V controller and Nanoscope software version 8.15 were utilized (Key Resource Table). All quantitative measurements were performed using standard conical tips (ScanAsyst Air, Bruker, Inc.). The tip radius is given by the manufacturer to be between 2 nm and 10 nm. The spring constant of cantilevers was measured using the thermal tuning method (Hutter and Bechhoefer, 1993; Maaloum, M. Lévy, 2002) and ranged from 0.3–0.7 N/m. The deflection sensitivity of the cantilevers was calibrated against clean silicon Safire. Measurements were made on leaf sections embedded in LR White (LRW) Resin (aromatic acrylic resin mixture; viscosity 8 cps) (see below) at room temperature. The sample was then positioned on an XY motorized stage and held by a magnetic clamp. Then, the AFM head was mounted on the stage and an approximated positioning with respect to the cantilever was done using the optical macroscope. The elasticity of the sample (demonstrated on the images) was estimated using the

DMT model (Derjaguin, Muller, Toropov modulus (Derjaguin et al., 1975)), which estimates the contact area between the tip of the AFM cantilever and the sample (elastically isotropic material) by quantifying the load forces and adhesion forces outside the contact area. Nanoscope software then converted the elasticity measurements to an image where stiffer areas were represented by brighter pixels and more elastic areas by darker pixels.

Resin embedding and sectioning

Leaf pieces (approx. 1 mm x 1 mm) were fixed in ice-cold fixation solution (4% Paraformaldehyde and 0.05% Glutaraldehyde dissolved in 100 mM phosphate buffer, pH 7.2) at 4°C overnight. The samples were washed 3 times for 10 min with 100 mM phosphate buffer and embedded in LRW resin, medium grade - catalyzed (TAAB essentials for microscopy, England, UK) according to the manufacturer's instructions (Key Resource Table). Serial paradermal ultrathin sections (thickness of 50 - 70 nm) were prepared using an ultramicrotome (RMC Power Tome & Reichert Ultracut Microtome) and mounted on formvar coated grids.

Immunolocalization for electron microscopy

Grids holding sample sections were incubated in blocking reagent (1% albumin from bovine serum (BSA) in Phosphate-buffered saline (PBS), SIGMA-ALDRICH) for 30 minutes, then in primary antibodies (Key Resource Table, A to F) diluted 10 times in blocking reagent for one hour, washed in PBS (10 min, 3 times), incubated in secondary antibodies (10 nm gold particles conjugated to goat either anti-mouse IgG or anti-rat IgG diluted 20 times in the blocking reagent (Key Resource Table), rinsed subsequently in blocking reagent, in PBS and in dH_2O (10 min, 6 times) and left to dry on filter paper (30 min). All these steps were carried out at room temperature. For better visualization in EM, sections on the grids were incubated with 5% uranyl acetate in the dark for 15 min, after which they were rinsed in dH_2O and left to dry on filter paper. Grids with sections were imaged using an electron microscope (JEOL 1230 TEM, accelerating voltage 80 kV, with a Gatan MSC 600CW 2k x 2k CCD camera).

Confocal microscopy image acquisition

For pavement cell shape analysis, the 3rd leaves of *Arabidopsis* were imaged on a confocal microscope (Zeiss LSM 780) after the leaves had been fixed overnight in a solution of absolute

ethanol and glacial acetic acid (9:1), rehydrated in descending ethanol concentrations (70%, 50%, 40%, 30%, 20%, 10%) and stored in 50% glycerol solution. Fixed leaves were treated with propidium iodide (Sigma-Aldrich) for visualization of the cell outline. At least 5 leaves and 50 cells per leaf from the middle of the leaf blade were analyzed from each line. The experiment was repeated three times.

Automated TEM image analysis

Plasma membrane borders were manually outlined using the software GIMP2.8.8 while gold particles within the cell wall were automatically detected and analyzed through scripts in Matlab (R2012b, The MathWorks, Inc., Natick, Massachusetts, United States), (Key Resource Table). The pixel size in each image was derived by manually marking the beginning and end of the scale bar and providing the length as input. The midline in the cell wall was extracted by applying a watershed transform on a distance transform calculated from the plasma membrane borders. The local curvature was measured along the midline by fitting a polygon to points on the midline 230 nm ahead of and behind the current midline point and calculating the curvature analytically for that polygon. The curvature vector was smoothed using a median filter of length 5 and the wall region was divided into straight and convex regions based on thresholding the curvature values on the midline. Suitable thresholds were chosen by visual assessment of several images and then kept constant for all images. Regions of the wall corresponding to midline pixels too close to the image border to calculate local curvature were excluded from the analysis. The numbers of pixels in the convex and straight regions, multiplied by the pixel size were used as area estimates.

In order to compensate for different contrast and intensity levels in the micrographs, the intensities within the wall region were linearly stretched between the 0.05 and 99.95 percentile intensity values.

Gold particles were detected as small dark spots surrounded by bright pixels. The image was inverted and pixels whose intensity was higher than 200 and at the same time had a local contrast of 60, calculated as the difference between the pixel intensity and the 15th darkest intensity value in a 5x5 neighborhood, were saved as potential gold particle pixels. Out of these potential gold particle pixels, the pixels with intensity higher than 86% of the highest intensity or a local contrast higher than 100, were saved as gold particle pixels. This marks pixels in small

bright regions with dark surroundings. Out of these only the brightest pixel within a radius of 2 pixels was kept as the center of a gold particle. The automatic gold detection results were visually assessed for each image and images where the detection was deemed too poor (too many false positives or negatives) were discarded from the analysis.

The distance for each gold particle to the two plasma membranes was simply derived by extracting that position's value in the two distance transforms (DTs) calculated from the two membranes respectively. The ratio was derived as the distance of the gold particle from one side of the plasma membrane divided by its total distance between both plasma membranes. This ratio gave the position of the gold particle expressed as a percentage. Then measurements were grouped into three groups according to how far the gold particle was located from one plasma membrane.

Cell shape analysis

Laser Scanning Confocal Microscope (LSCM) raw images were pre-processed in order to enhance cell wall signal using the following ImageJ 1.49p (Schindelin et al., 2012; Schneider et al., 2012) functions: Subtract background and Enhance contrast. Images were segmented using CellSeT (Pound et al., 2012) (Key Resource Table). Stomata were then filled with background. Area and Circularity were measured for each cell using the Analyze particles function in ImageJ. A circularity value of 1.0 corresponds to a perfect circular shape, while a smaller value indicates a relative level of interdigitation. Lobe number was estimated automatically using Skeletonize function and the plugin Analyze Skeleton. Cell area values were log transformed to reduce skewness and compared using ANOVA and Tukey's test in R software. Circularity and lobe number were compared for cells having log (cell area) value between 2.62 and 3.10 (Col-0 and associated mutants) and 2.42 and 3.05 (WS and associated mutants) using ANOVA and Tukey's test in R software.

Finite Element Model simulation

The model of the thin walled initially square "cell" was built and simulated using Abaqus (Dassault Systemes Simulia Corp.) v6.12 (Key Resource Table). This software solves continuous mechanic equations by a Finite Elements Method (FEM), which, in general, is based on linearization and minimization of a strain energy density. The particular form of this energy

depends on the material model. In our simulations we used a linear elastic material (Saint Venant-Kirchhoff model) resulting in the strain energy W in the form

$$W(\acute{\varepsilon}) = \frac{E\nu}{(1+\nu)(1-2\nu)}[tr(\acute{\varepsilon})]^2 + \frac{E}{2(1+\nu)}tr(\acute{\varepsilon}^2),$$

where $\acute{\varepsilon}$ is a Lagrangian Green strain tensor, E is the Young elastic modulus and ν is the Poisson coefficient.

We used Poisson coefficient 0.3 and Young modulus 50 kPa for weak composite material and 100kPa for hard material to test the values in the range reported experimentally (Chanliaud et al., 2002; Hayot et al., 2012; Nezhad et al., 2013) and representing the elasticity difference of about 50%. The homogenous material Young modulus was chosen as the average of hard and weak materials Young moduli, 90 kPa.

The square "cell" of dimensions 100 μm by 100 μm, depth 50 μm, and wall thickness of 2 μm, was modeled with the use of eight-node brick elements with reduced integration. Mesh independence of our result was tested by using different coarsens meshes with at least 4 elements across the wall thickness. For single slab simulations (Figure 2A-D) we used the same dimensions, 100 μm × 50 μm × 2 μm, and the same material properties as for the Figure 2E-G simulations.

We assumed that the turgor pressure in all considered cells is the same so the cumulative effect of it on the tissue scale reduces to tensional forces on the anticlinal walls. This allows considerably reducing computational complexity of the model and improving stability of the simulation. To confirm that presence of compressive forces across the wall thickness coming from turgor pressure do not alter our conclusions we performed a simulation of bending of single wall segment of inhomogeneous composite wall with pressure loads on both sides of the wall (Figure 2K, L) and could not detect any influence of the turgor pressure on the bending process.

The forces used to stretch the walls were in the order of 10 nN and were applied to the four free ends of the wall segments (Figure 2E-G) as surface tractions following rotation. The opposite ends of the wall segments were constrained in the direction of loading forces. They were free to move in a perpendicular direction providing x- and y-symmetry boundary conditions for these walls respectively. The bottom edge of the structure was constrained in the z direction.

QUANTIFICATION AND STATISTICAL ANALYSIS

Statistical analyses were preformed using Microsoft Excel and R software (Key Resource Table). Statistics were performed using ANOVA and Tukey's test. Means ± SE are shown, n values are displayed on the graphs (Figure 1, S1). Statistical significance was tested by Student's T-test. Error bars correspond to ± SE (Figure 4-7, S5, S7). Significance was defined as *$P < 0.05$; **$P < 0.01$; ***$P < 0.001$.

DATA AND SOFTWARE AVAILABILITY

KEY RESOURCE TABLE

REAGENT or RESOURCE	SOURCE	IDENTIFIER
Antibodies		
Mouse monoclonal CCRC M1	CarboSource	N/A
Mouse monoclonal CCRC M89	CarboSource	N/A
Rat monoclonal JIM5	PlantProbes	Cat#JIM5
Rat monoclonal JIM7	PlantProbes	Cat#JIM7
Rat monoclonal LM5	PlantProbes	Cat#LM5
Rat monoclonal LM6	PlantProbes	Cat#LM6
Green Fluorescent Protein-CMB3	Nzytech	14021
EM Goat anti-Rat IgG: 10 nm Gold	BBInternational	EM.GAT
Goat anti-Rat IgG: 10 nm Gold	TAAB	GEM027
EM Goat anti-Mouse IgG: 10 nm Gold	BBInternational	N/A
Goat anti-Mouse IgG (H+L): 10 nm Gold	TAAB	GEM025
Chemicals, Peptides, and Recombinant Proteins		
Paraformaldehyde	Sigma-Aldrich	N/A
Glutaraldehyde	Sigma-Aldrich	N/A
Albumin from bovine serum (BSA)	Sigma-Aldrich	N/A
LRW resin, medium grade - catalyzed	TAAB essentials for microscopy, England, UK	N/A
propidium iodide	Sigma-Aldrich	N/A
Deposited Data		
Experimental Models: Organisms/Strains		
Arabidopsis thaliana (Col-0)	N/A	N/A
Arabidopsis thaliana (WS)	N/A	N/A
CA-rop2	(Fu et al., 2002)	N/A
gal10-1	(Sampedro et al., 2012)	N/A
gals1	(Liwanag et al., 2012)	N/A
35S::GALS-YFP	(Liwanag et al., 2012)	N/A
gsl8-2	(Chen et al., 2009)	N/A
kor1-1	(Nicol et al., 1998)	N/A
mur1-2	(Bonin et al., 1997)	N/A
mur2-1	(Reiter et al., 1997)	N/A
mur3-1	(Reiter et al., 1997)	N/A
mur4-1	(Reiter et al., 1997)	N/A
pom1-2	(Zhong et al., 2002)	N/A
prc1-1	(Desnos et al., 1996)	N/A
qua1-1	(Bouton et al., 2002)	N/A
qua2-1	(Bouton et al., 2002)	N/A
xxt1/xxt2	(Cavalier et al., 2008)	N/A
xxt5	(Zabotina et al., 2008)	N/A
xxt1/xxt2/xxt5	(Zabotina et al., 2012)	N/A
Cinnamonum camphora	University of Wroclaw	N/A
Software and Algorithms		
R	https://www.r-project.org/	N/A
CellSet 1.5.1.0	https://www.cpib.ac.uk/tools-resources/software/cellset/	N/A
Matlab R2012b, The MathWorks	https://mathworks.com/products/matlab.html	N/A
Nanoscope version 8.15, Bruker	https://www.bruker.com	N/A

Abaqus (Dassault Systemes Simulia Corp.) v6.12.	https://www.3ds.com/products-services/simulia/products/abaqus/	N/A
Other		

Table

Sample ID	stiffer cell wall zone	stiffness difference (%)
1	straight	3.62
2	curved	39.00
3	curved	7.35
4	curved	28.53
5	curved	13.55
6	curved	16.77
7	curved	11.49
8	curved	11.23
9	curved	16.65
10	straight	1.10
11	straight	5.78
12	curved	5.60
13	curved	37.90
14	curved	17.60
15	curved	41.50
16	curved	37.50
17	curved	13.50
18	curved	10.80
19	curved	1.50
20	curved	6.85

Sample ID	stiffer cell wall zone	stiffness difference (%)
1	straight	6.78
2	straight	3.58
3	straight	1.06
4	straight	1.28
5	straight	1.31
6	straight	2.83
7	straight	5.63
8	straight	4.44
9	straight	0.54
10	straight	1.67
11	straight	3.56
12	straight	8.55
13	straight	2.07
14	straight	7.27
15	straight	5.69

Sample ID	stiffer cell wall zone	stiffness difference (%)
1	concave	16.22
2	concave	6.84
3	concave	4.37
4	convex	1.10
5	concave	4.08
6	concave	6.52
7	convex	13.40
8	concave	1.10
9	concave	11.21
10	convex	7.20
11	concave	8.55
12	concave	8.51
13	convex	12.20
14	convex	53.90
15	concave	23.70
16	concave	12.78
17	convex	24.35
18	concave	4.78
19	concave	12.62
20	concave	27.70
21	convex	31.20
22	concave	6.47
23	concave	7.80
24	concave	19.80
25	concave	7.86
26	convex	18.20

Sample ID	stiffness difference (%)
1	12.77
2	0.70
3	1.89
4	4.73
5	16.77
6	10.34
7	7.03
8	3.10
9	16.03
10	2.89
11	17.95
12	27.48
13	3.86
14	5.05
15	0.38

Sample ID	stiffness difference (%)
1	4.55
2	0.53
3	1.63
4	1.59
5	4.31
6	0.31
7	2.96
8	0.49
9	1.71
10	1.45
11	3.3
12	5.05
13	4.29
14	6.77
15	2.93

Figure 1

Click here to download Figure Figure 1-PC.tif ⬇
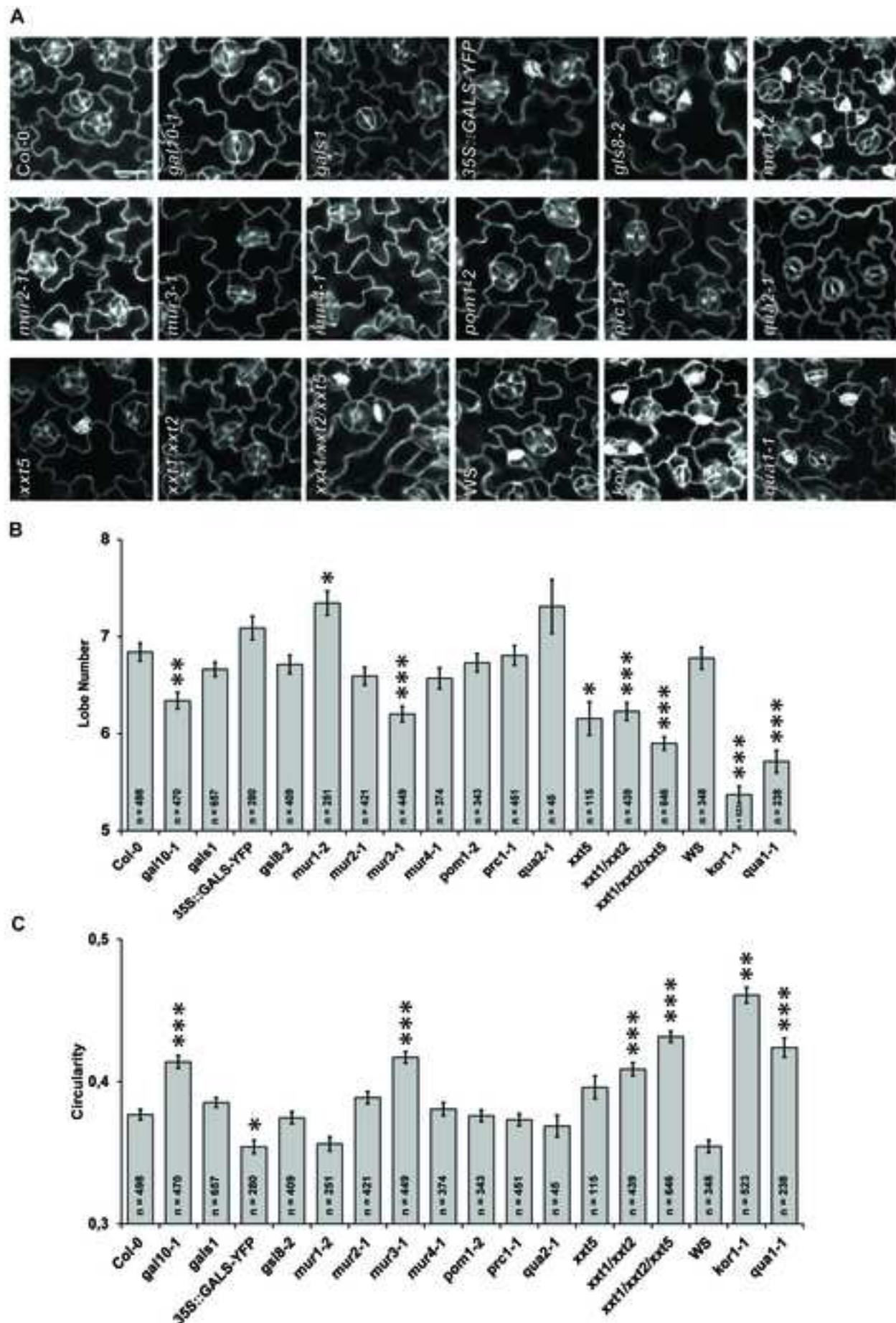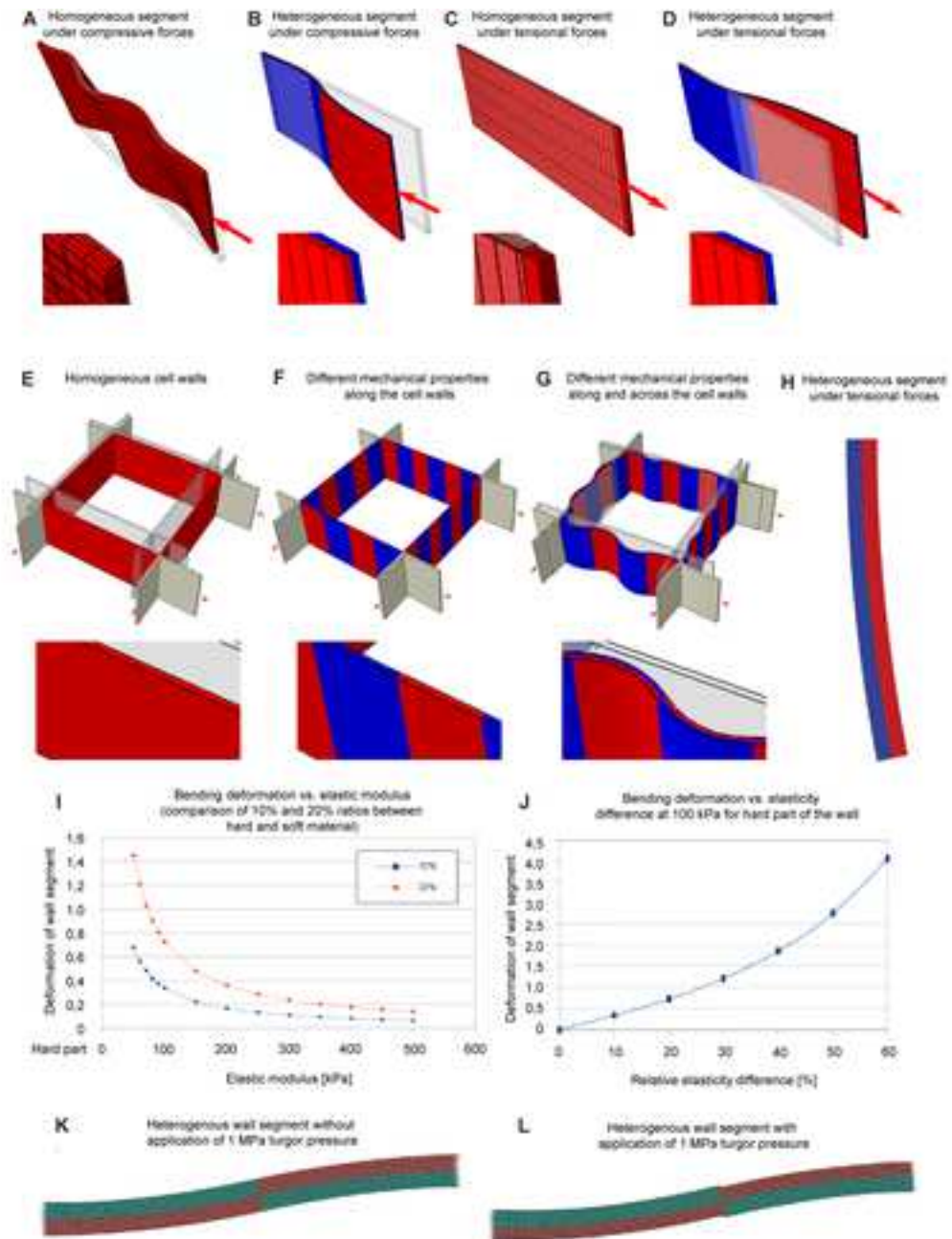
Figure 1.

Figure 2

Figure 2.

A Measured cell wall regions
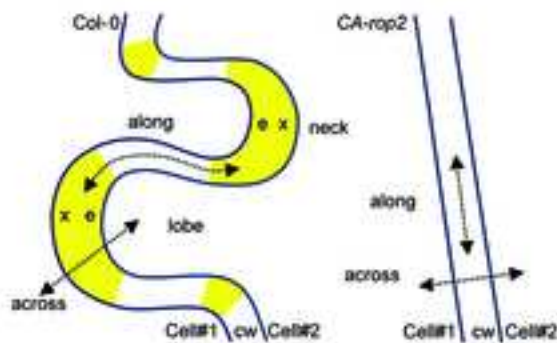
B AFM image with positions of ROIs on two sides (e=concave and x=convex) along the cell walls (1-18)
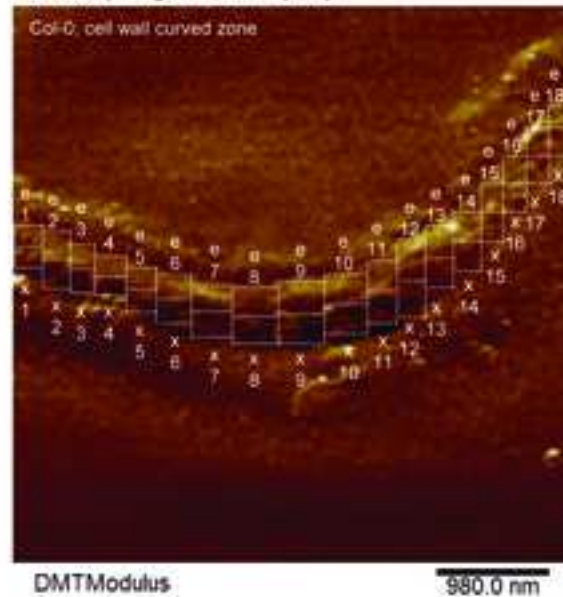
C Averages of stiffness measured in different ROIs shown in B

concave (e)	avg	SE	n	convex (x)	avg	SE	n	% stiffness (e)/(x)
e1	92,0	±7,1	35	x1	77,5	±1,5	43	18,7
e2	94,5	±1,6	49	x2	75,9	±1,3	56	24,5
e3	94,7	±1,5	35	x3	75,7	±1,7	42	25,1
e4	93,8	±1,2	40	x4	75,0	±2,2	48	25,1
e5	91,9	±1,2	48	x5	76,1	±1,8	48	20,7
e6	91,2	±1,1	54	x6	75,6	±1,6	54	20,7
e7	92,2	±2,1	50	x7	76,1	±1,5	70	21,2
e8	86,6	±1,1	72	x8	76,0	±1,3	72	14,2
e9	91,8	±1,3	72	x9	75,4	±0,7	84	21,7
e10	90,3	±1,2	96	x10	73,0	±1,7	96	23,8
e11	94,4	±1,1	56	x11	78,7	±1,7	56	20,0
e12	98,1	±1,6	63	x12	80,4	±1,3	63	22,1
e13	95,7	±4,7	49	x13	84,4	±1,7	49	13,5
e14	96,1	±3,9	49	x14	86,3	±2,0	42	11,4
e15	95,3	±5,2	36	x15	122,5	±25,4	36	-22,2
e16	89,7	±1,1	42	x16	90,3	±2,5	42	-0,7
e17	109,2	±8,9	36	x17	87,1	±1,4	36	25,4
e18	96,6	±7,9	42	x18	100,9	±10,1	49	-4,3

D Stiffness measured in concave(e) and convex(x) regions along the walls (1-18) in different ROIs shown in B
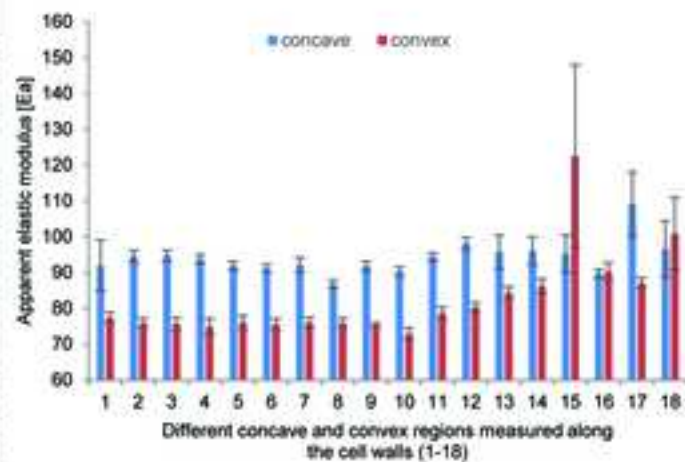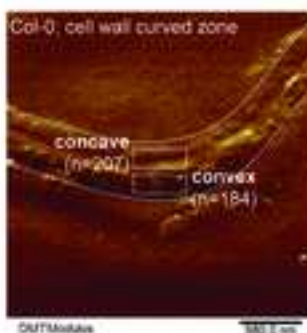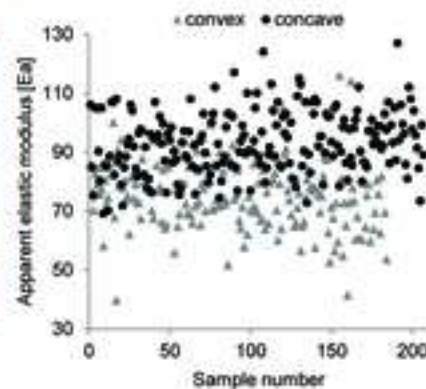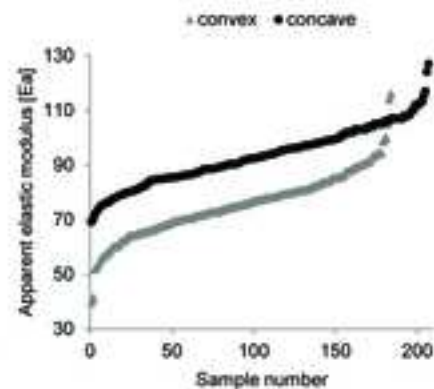
E AFM image with positions of ROIs on two sides of the cell wall

F Distribution of the stiffness between convex and concave cell wall regions depicted in E

G Normal distribution of the stiffness between convex and concave cell wall regions depicted in E
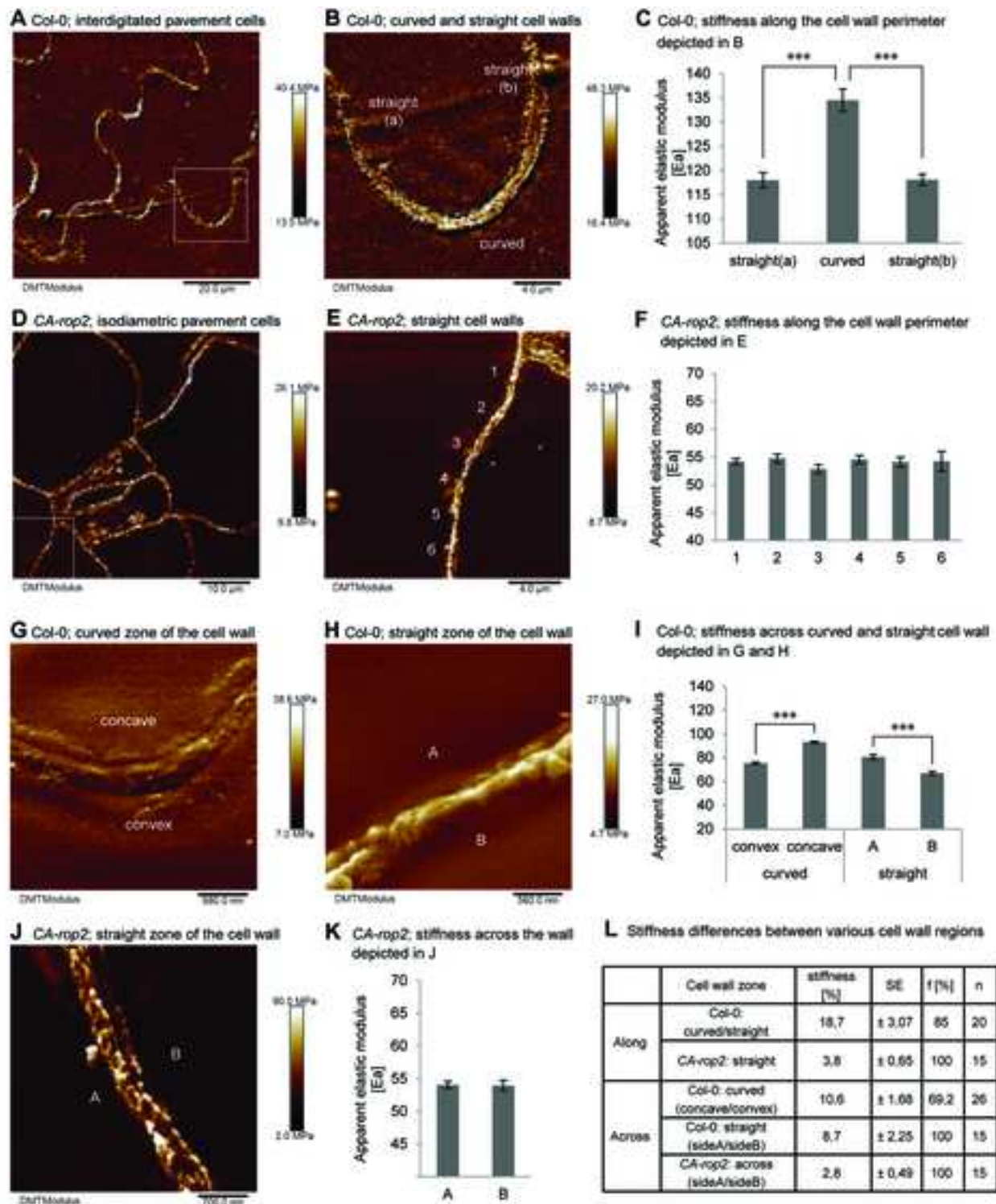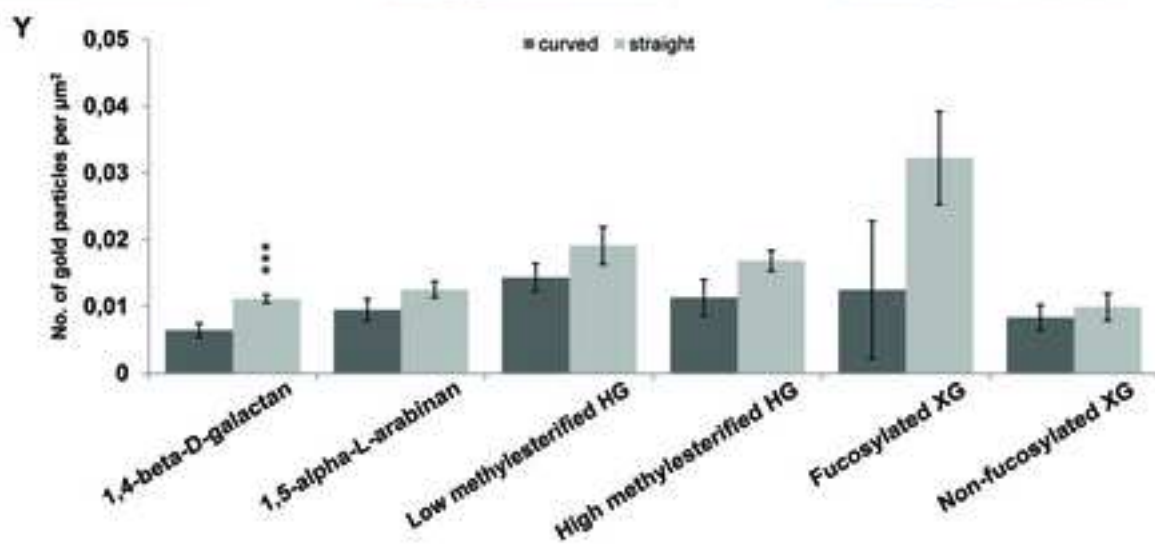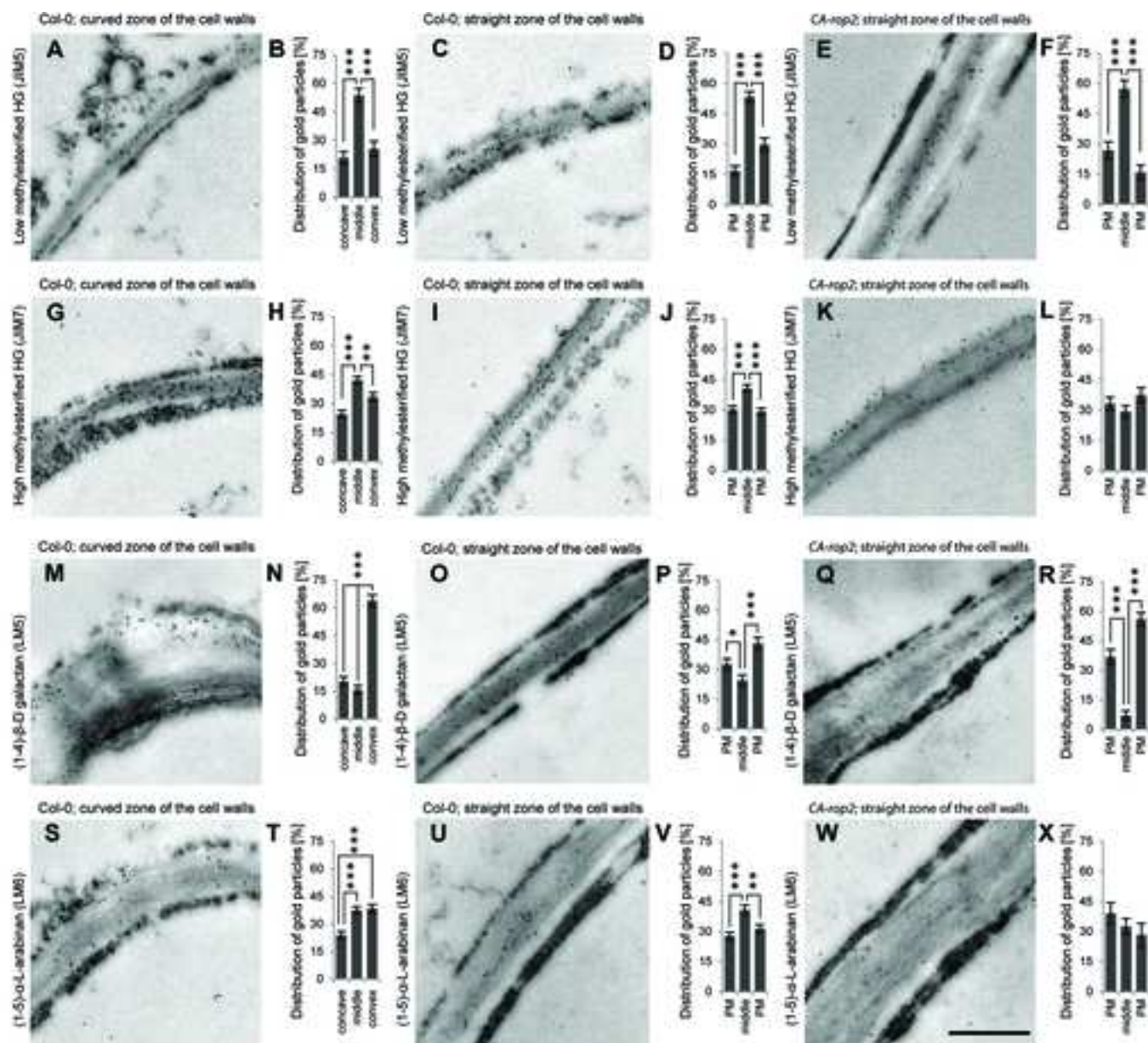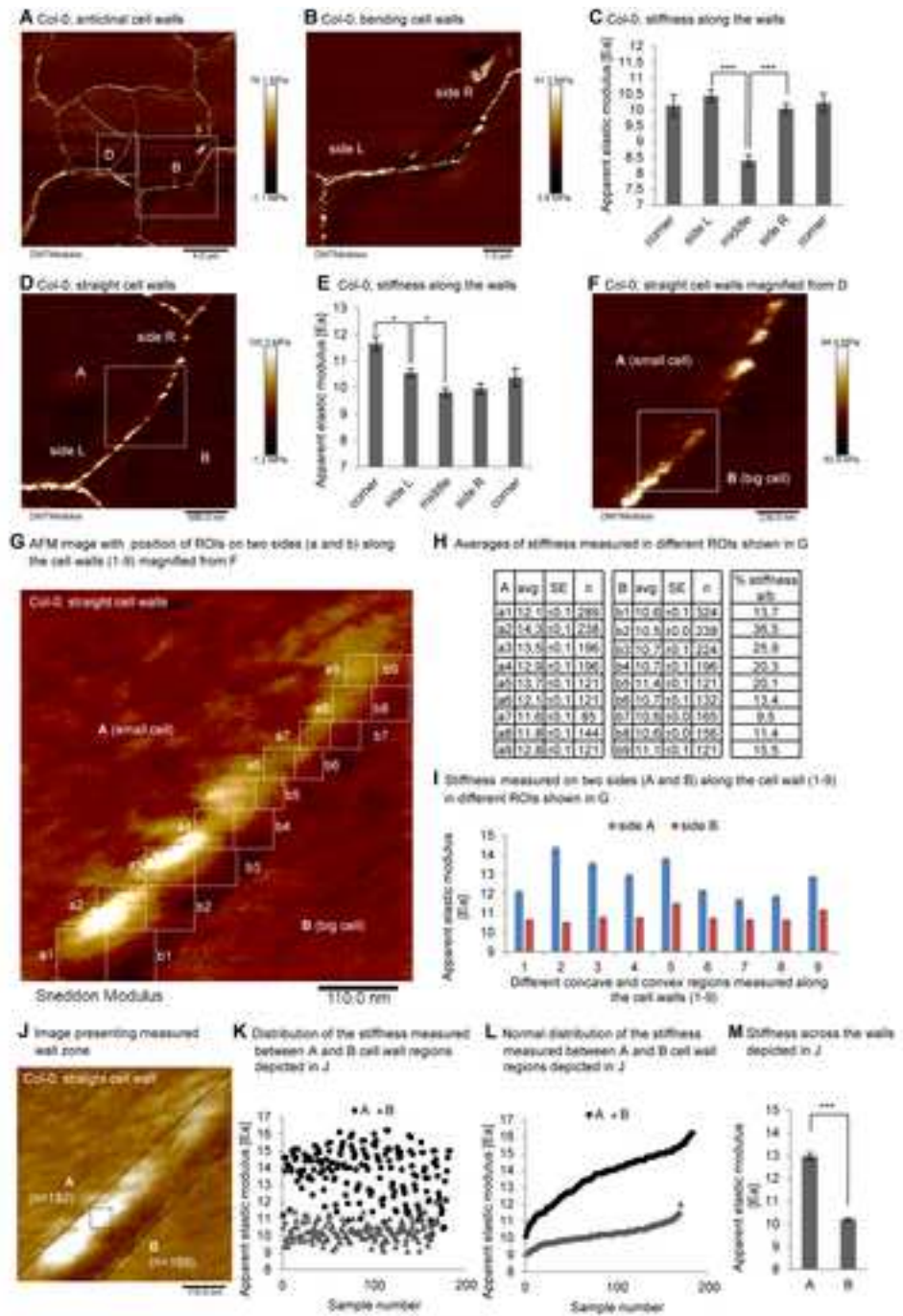
Figure 3.

Figure 4

Figure 4.

Figure 5   Click here to download Figure Figure 5-EM.tif ⬇

Figure 5.

Figure 6

Click here to download Figure Figure 6-AFMyoung.tif

Figure 6.

Figure 7.